Dynamic patterns of compaction in brittle porous media

François Guillard[1], Pouya Golshan[2], Luming Shen[1], Julio R. Valdes[2], and Itai Einav[1,3]
(Dated: June 29, 2015)

Brittle porous media exhibit a variety of irreversible patterns during densification, including stationary and moving compaction bands in rocks[1–3], foams[4], cereal packs[5] and snow[6]. We have recently found moving compaction bands in cereal packs[5]; similar bands have been detected in snow[6]. However, the question of generality remains – under what conditions may brittle porous media disclose other densification patterns? Here, using a new heuristic lattice spring model undergoing repeated crushing events, we first predict the possible emergence of new forms of dynamic compaction patterns; we then discover and confirm these new patterns experimentally in compressed cereal packs. In total, we distinguish three observed compaction patterns: (i) short-lived erratic compaction bands, (ii) multiple oscillatory propagating compaction bands, reminiscent of critical phenomena near phase transitions, and (iii) diffused irreversible densification. The manifestation of these three different patterns is mapped in a phase diagram using two dimensionless groups that represent fabric collapse and external dissipation.

Compaction of brittle porous media is of central importance in industry and science, and has many ramifications, from destruction waves during meteoritic impacts[7] to formation of density heterogeneities in pharmaceutical pills[8] and permeability barriers in rocks[9,10]. Previous work on brittle porous media has generally revealed two forms of compaction patterns: stationary and oscillatory propagating compaction bands. Specifically, stationary compaction bands with localised intense volumetric strain rate have been frequently observed in a wide range of brittle porous materials, including rocks[1–3], foams[4] and honeycomb materials[11]. The formation of such bands has been rationalised mathematically using continuum models of viscoplasticity[12,13] or breakage mechanics[14,15], with the latter connecting the process directly to the physics of grain breakage and pore collapse.

The formation of oscillatory propagating compaction bands in porous media was discovered more recently by Valdes et al.[5], via uniaxially confined compression experiments on puffed rice packs. Similar to stationary compaction bands, the material within these bands experienced high volumetric strain rates accommodated by severe grain breakage and pore collapse. By comparing experiments on material placed in containers with different boundary roughness, this work motivated a connection between compaction dynamics to how energy is dissipated outside.

More recently, similar experiments on dry foamy snow[6] also revealed oscillatory propagating compaction bands, although with only one or two oscillations per test (this will be discussed later, in Fig. 2(g-i)). This form of com-

paction was captured using a phenomenological continuum model for snow, with an assumed elastoplastic yield function, power-law density dependence, shear-induced bond failure, strength recovery due to sintering, and non-locality of damage[6]. The need for these assumptions indicates that the underlying mechanisms that control the emergence of oscillatory compaction bands are not clear yet.

In this paper we present experiments that unfold novel compaction patterns in brittle porous media. We show that all the observed patterns can be explained using a simple lattice spring model. We then map the manifested patterns in terms of a phase diagram that covers system and material parameters, applicable for brittle porous media in general.
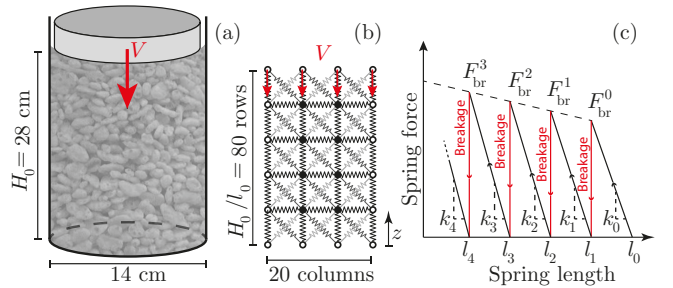

FIG. 1. **Experimental and numerical configurations. a** Experimental configuration. **b** Lattice spring model. **c** Force-displacement relation for the springs undergoing repetitive breakage events during loading. Unloading follows the loading curve until the spring length equals the relaxed length l_i that corresponds to the number of breakage events i; beyond that point the force is set to zero.

The experimental configuration is schematically shown in Fig. 1a. It consists of a transparent cylinder initially filled with puffed rice cereal to a height H_0. The material is then compressed from the top using a circular piston with a constant velocity V till about 50% strain

[1] Particles and Grains Laboratory, School of Civil Engineering, The University of Sydney, Sydney, NSW 2006, Australia.
[2] Geo-Innovations Research Lab; Department of Civil, Construction, and Environmental Engineering; San Diego State University.
[3] Dept of Civil, Environ & Geomatic Eng, Faculty of Engineering Science, University College London.
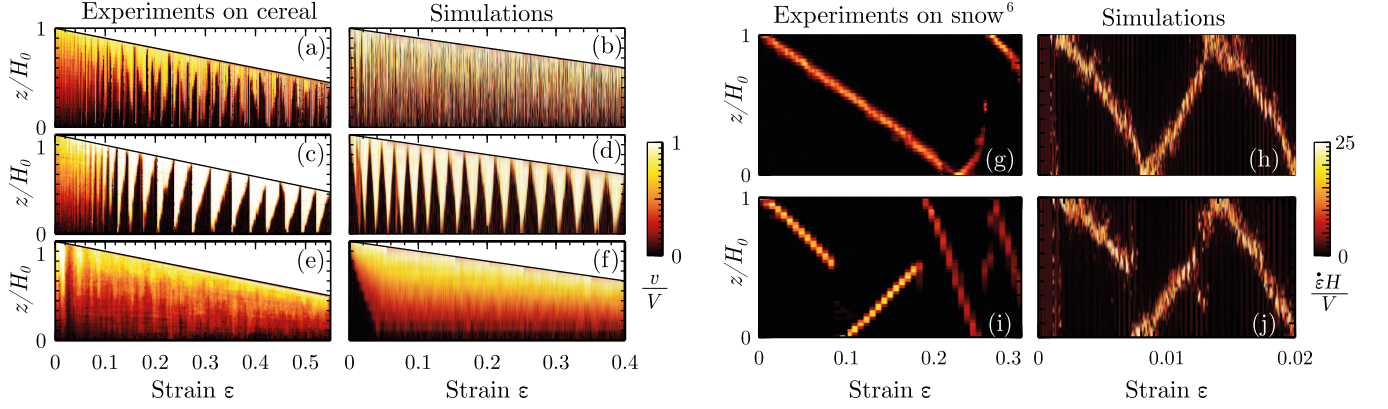
FIG. 2. **Patterns of compaction from experiments and numerical model**. **a-f** Contours of local velocity v normalised by piston velocity V. **a,c,e** Experiments with $V = 0.013\,\mathrm{mm.s^{-1}}$, $1.3\,\mathrm{mm.s^{-1}}$, and $300\,\mathrm{mm.s^{-1}}$, respectively. **b,d,f** Model simulations with $V = 5 \cdot 10^{-6}$, $2 \cdot 10^{-5}$, and $7 \cdot 10^{-5}$, respectively (with $k_0 = 2 \cdot 10^{-3}$, $F_0^{\mathrm{br}} = 2 \cdot 10^{-6}$, $\eta = 1 \cdot 10^{-3}$). **g-i** Normalised local strain rate $\dot{\epsilon}$ in **g,i** compaction experiments on snow for $V = 1.125$ and $5\,\mathrm{mm.s^{-1}}$, respectively (adapted from[6]); **h,j** Simulations with $V = 2.45 \cdot 10^{-6}$ and $2.5 \cdot 10^{-6}$ (for $k_0 = 2.5 \cdot 10^{-4}$, $F_0^{\mathrm{br}} = 2.5 \cdot 10^{-7}$, $\eta = 2.5 \cdot 10^{-4}$).

$\epsilon = 1 - H/H_0$. During loading we record the side of the cylinder's shaft using a regular or high speed video camera, depending on the piston velocity. Pictures are then processed using Particle Image Velocimetry to analyse the material's velocity field. Since the compression is purely axial, all velocities at a given height are averaged, and thus, the axial velocity patterns are presented as a function of the axial depth and time.

Figs. 2(a,c,e) are the spatio-temporal plots of the local material velocity $v(z)$ normalised by the piston velocity V for three different V. Clearly, the way the material densifies depends strongly on V. At intermediate V (Fig. 2c), we recover the oscillatory propagating compaction bands found previously[5]. We notice that a single period of oscillation starts with a compaction band that nucleates at the bottom; the band then propagates up until it reaches the top, and then reemerges at the bottom, to start a new oscillation period. Such bands split the sample into an upper material block that moves down with a velocity close to the piston velocity $v(z) \sim V$ and a lower block with $v(z) \sim 0$; as shown by[5], these two material blocks are separated by a narrow compaction band of intense velocity gradient. Under lower and higher piston velocities we unravel different forms of compaction. Under lower V the material experiences short-lived and localised compaction appearing erratically in space (Fig. 2a). Under higher V the material compacts almost homogeneously with $v(z) \simeq \frac{V}{H}z$.

In parallel to performing experiments, we developed a heuristic microstructural model to recover the oscillatory compaction patterns at the intermediate velocity. In carrying out computations, the model led us to detect the new patterns corresponding to the lower and higher velocities, which we then confirmed experimentally. Building on a spring lattice system, our model extends a previous quasi-static massless model that recovers stationary compaction bands[16,17]. Here, mass is included to tackle

dynamic phenomena and the springs can take repetitive breakage events to model highly porous brittle material. The lattice is shown Fig. 1b, and the response of the spring elements follow the force-length diagram in Fig. 1c (see detailed information in Methods). The springs transmit elastic forces to the masses; these masses carry a further dissipative force given by global damping. Use of either local damping or friction is discussed in Supplementary to further support the generality of our conclusions.

Figs. 2(b,d,f) present results from the lattice simulations with increasing V, which qualitatively agree with the experimental results of Fig. 2(a,c,e). We note that unlike the experimental oscillations in Fig. 2(c) the theoretical ones in Fig. 2(d) begin earlier and propagate symmetrically. Differences as such develop from unavoidable experimental heterogeneities, both through initial grain rearrangements and from statistical variation in grain strengths[18]. Indeed, although most experiments showed upward band propagations, a few others did exhibit either symmetrical or downward propagation.

We propose that such patterns are characteristics of general brittle porous media; the manifested compaction pattern depends on both material and system parameters. A first support for this generic claim is given in Supplementary, which shows similar predictions for alternative force dissipation mechanisms ($viz.$ similar patterns arise when one employs local damping or friction instead of global damping). A second support is given by comparing model simulations with experiments; this time on dry foamy snow, given by Barraclough et al.[6] (see Figure 2(g,i)), who adopted an experimental configuration similar to that of Valdes et al.[5] (shown in Fig. 1a). Our simulations yield similar patterns already under much smaller strains (see Figure 2(h,j)), including the featuring of incomplete upward and downward band propagations. The compliance and brittleness of puffed rice packs are

much larger than those of snow, and as such, puffed rice can accommodate many more oscillations; these properties allow us to identify the compaction patterns in Figs. 2(a,e).

Next, we use the model to unfold how breakage controls the various compaction patterns; an objective that is practically impossible to probe experimentally. For this purpose, we examine the breakage rate β as a function of depth z and strain ϵ by computing the average number of breakage events per spring between time steps. We normalise β using a 'breakage time' τ_{br}^0, *i.e.*, the typical time between two consecutive breakage events (see Methods).

Fig. 3 shows the scaled breakage rate $\beta\tau_{\mathrm{br}}^0$ along z and ϵ for five simulations with distinct identifiable patterns. Specifically, Figs. 3(a,b,e) correspond to Figs. 2(a,c,e). It is clear by comparisons, especially between Fig. 3b and Fig. 2c, that compaction band motions synchronise with breakage rate. There is almost no breakage outside the bands, whereas inside, the breakage rate is the highest. Under the lowest imposed velocity (Fig. 3a), breakage develops irregularly in space and time, which explains why the corresponding velocity field reveals erratic and short-lived compaction bands. Under the highest velocity, the breakage develops almost continuously and uniformly (Fig. 3e), which explains why the corresponding velocity field is almost homogeneous. We detect further sub-patterns of oscillatory compaction bands – with bifurcation into more than a single oscillating band, as shown in Fig. 3c (two fronts) and 3d (three fronts). These intricate velocity fields are not observed experimentally yet; but this may be explained since the range of parameters to observe such behaviours is small for experimental detection (as we shall show in Fig. 4).

Apart from the breakage time τ_{br} mentioned above, two other time scales are identified from all the model parameters, including an elastic time τ_{el} and the viscous time τ_η. The elastic time defines the characteristic time required from an elastic wave to travel through the whole sample, and the viscous time denotes the typical time required for mass m to slow down its motion due to the global damping. In total, the system is defined in terms of the following times:

$$\tau_{\mathrm{br}} = \frac{F_{\mathrm{br}}}{kl}\frac{H}{V} \;\; ; \;\; \tau_{\mathrm{el}} = \frac{H}{l}\sqrt{\frac{m}{k}} \;\; ; \;\; \tau_\eta = \frac{m}{\eta} \tag{1}$$

where the index 'i' has been omitted to simplify the text. Given these three times we can define two non-dimensional groups *via* time ratios:

$$B_{\mathrm{el}} = \frac{\tau_{\mathrm{br}}}{\tau_{\mathrm{el}}} = \frac{F_{\mathrm{br}}}{V\sqrt{km}} \;\; ; \;\; B_\eta = \frac{\tau_{\mathrm{br}}}{\tau_\eta} = \frac{F_{\mathrm{br}}H\eta}{klVm} \tag{2}$$

to be called the 'elasto-breakage number' and 'visco-breakage number', respectively.

Note that since the various parameters change during one simulation, B_{el} and B_η change too. Specifically, over
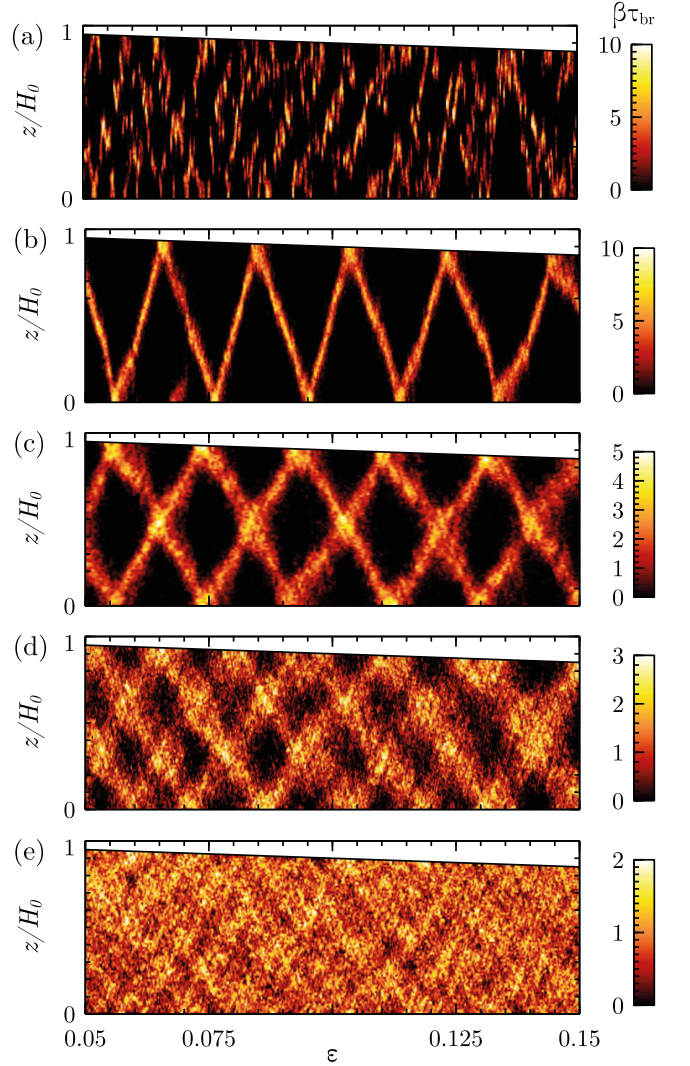

FIG. 3. **Breakage patterns.** Normalised breakage rate β as a function of height z and strain ϵ for various piston velocities: **a-e** $V = 5\cdot10^{-6}$, $2\cdot10^{-5}$, $4\cdot10^{-5}$, $5.2\cdot10^{-5}$, and $7\cdot10^{-5}$. All other parameters remain consistent with Fig. 2.

time the height H decreases and the number of breakage events increases (i grows). Thus, k_{i} and $F_{\mathrm{br}}^{\mathrm{i}}$ increase as well. This may cause switches between the behavioural regimes, as observed in a few simulations. Therefore, the phase diagram in Fig. 4 collates only the first identifiable compaction regimes defined by the initial parameter values $(F_{\mathrm{br}}^0, k_0, l_0, H_0, \eta, m, V)$, in terms of B_{el} and B_η.

The compaction zones are short-lived and appear erratically when B_η is high because the motion after a local breakage event has sufficient time to slow down by viscosity before further breakage, and since the steady state stress is essentially uniform throughout. Conversely, at very low B_η there is not enough time for relaxation, and thus the whole sample undergoes crushing almost simultaneously. Intermediately (between these two extreme regimes) we find oscillatory propagating compaction bands with bifurcation dependent on the value
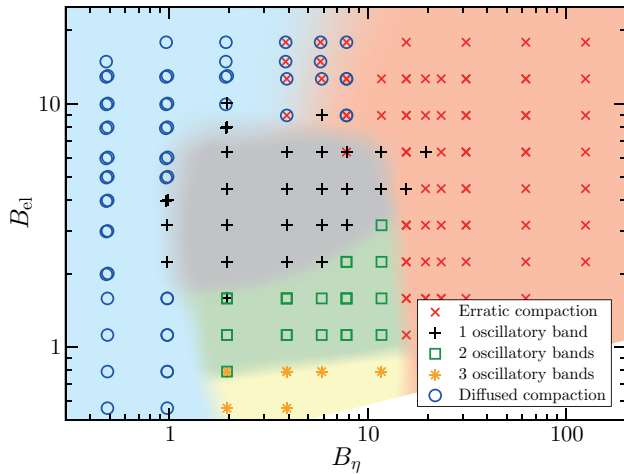
FIG. 4. **Dimensionless phase diagram of compaction regimes.** Shadings are added in the background to highlight the separation between the observed simulation patterns.

of B_{el}. As B_{el} gets smaller we move from a single oscillatory band to two or three bands, but the parametric resolution for capturing such bands narrows. This behaviour is reminiscent of critical phenomena near phase transitions.

In conclusion, this paper presents experiments that unfold compaction patterns inherent to brittle porous media, and a new heuristic spring lattice model that undertakes repetitive breakage events to explain those patterns. The model also captures other previously observed regimes of compaction in experiments on rocks, puffed rice packs and dry foamy snow. We note that during confined compaction, these materials undertake both internal fabric collapse (e.g., breakage) and external dissipation (e.g., viscous damping), as was underpinned by the model. We argue that although the physics that control these two processes may vary between materials, the mapping of the compaction patterns provided in this paper is generic for brittle porous media (see further support in Supplementary).

Brittleness adds complexity to the dynamics of granular flows[19] and can alter the propagation of density fronts often observed during the flow of loose, non-brittle granular media[20–22]. Finally, we recall another form of strain localisation that occurs during the extension of metallic alloys – known as the Portevin - Le Châtelier (PLC) effect[23–25]. In this case, the motion of atomic impurities during the compression leads to a jerky flow of the material. The compaction band formed in the material (PLC type A) does not remain steady, but travels back and forth in the medium, leading to the observation of a stress drop when the band reaches one end. Therefore, since this is similar to the observations in Figs. 2c and 2d, our results in brittle porous media may provide a new perspective into the study of the PLC effect in alloys.

[1] Olsson, W. A., Quasistatic propagation of compaction fronts in porous rock. *Mechanics of Materials* **33**, 659–668 (2001).

[2] Vajdova, V. & Wong, T. F., Incremental propagation of discrete compaction bands: Acoustic emission and microstructural observations on circumferentially notched samples of Bentheim. *Geophysical Research Letters* **30**, 1–4 (2003).

[3] Baud, P., Klein, E. & Wong, T. F., Compaction localization in porous sandstones: Spatial evolution of damage and acoustic emission activity. *Journal of Structural Geology* **26**, 603–624 (2004).

[4] Bastawros, A.-F., Bart-Smith, H. & Evans, A. G., Experimental analysis of deformation mechanisms in a closed-cell aluminum alloy foam. *Journal of the Mechanics and Physics of Solids* **48**, 301–322 (1999).

[5] Valdes, J. R., Fernandes, F. L. & Einav, I., Periodic propagation of localized compaction in a brittle granular material. *Granular Matter* **14**, 71–76 (2011).

[6] Barraclough, T. W., Blackford, J. R., Liebenstein, S., Sandfeld, S., Stratford, T. J., Weinländer, G. & Zaiser, M., Propagating compaction bands in confined compression of snow : Experiment and Modelling. *arXiv:1501.0218* (2015).

[7] Love, S. G., Hörz, F. & Brownlee, D. E., Target porosity effects in impact cratering and collisional disruption. *Icarus* **105**, 216–224 (1993).

[8] Wu, C. Y., Ruddy, O. M., Bentham, A. C., Hancock, B. C., Best, S. M. & Elliott, J. A., Modelling the mechanical behaviour of pharmaceutical powders during compaction. *Powder Technology* **152**, 107–117 (2005).

[9] David, C., Wong, T. F., Zhu, W. & Zhang, J., Laboratory measurement of compaction-induced permeability change in porous rocks: Implications for the generation and maintenance of pore pressure excess in the crust. *Pure and Applied Geophysics* **143**, 425–456 (1994).

[10] Olsson, W. A., Theoretical and experimental investigation of compaction bands in porous rock. *Journal of Geophysical Research* **104**, 7219 (1999).

[11] Papka, S. & Kyriakides, S., Experiments and full-scale numerical simulations of in-plane crushing of a honeycomb. *Acta Materialia* **46**, 2765–2776 (1998).

[12] Rudnicki, J. & Rice, J., Conditions for the localization of deformation in pressure-sensitive dilatant materials. *Journal of the Mechanics and Physics of Solids* **23**, 371–394 (1975).

[13] Veveakis, E. & Regenauer-Lieb, K., Cnoidal waves in solids. *Journal of the Mechanics and Physics of Solids* **78**, 231–248 (2015).

[14] Das, A., Nguyen, G. D. & Einav, I., The propagation of compaction bands in porous rocks based on breakage mechanics. *Journal of Geophysical Research: Solid Earth* **118**, 2049–2066 (2013).

[15] Das, A., Tengattini, A., Nguyen, G. D., Viggiani, G., Hall, S. A. & Einav, I., A thermomechanical constitutive model for cemented granular materials with quantifiable internal variables. Part II - Validation and localization analysis. *Journal of the Mechanics and Physics of Solids* **70**, 382–

405 (2014).

16. Katsman, R., Aharonov, E. & Scher, H., Numerical simulation of compaction bands in high-porosity sedimentary rock. *Mechanics of Materials* **37**, 143–162 (2005).

17. Kale, S. & Ostoja-Starzewski, M., Elastic-plastic-brittle transitions and avalanches in disordered media. *Physical Review Letters* **112**, 045503 (2014).

18. McDowell, G. R. & Humphreys, A., Yielding of granular materials. *Granular Matter* **4**, 1–8 (2002).

19. Marks, B. & Einav, I., A mixture of crushing and segregation : The complexity of grainsize in natural granular flows. *Geophysical Research Letters* **42**, 274–281 (2015).

20. Wu, X. L., Måløy, K. J., Hansen, A., Ammi, M. & Bideau, D., Why hour glasses tick. *Physical Review Letters* **71**, 1363–1366 (1993).

21. Pennec, T. L., Ammi, M., Messager, J. C. & Valance, A., Dynamics of density waves in a two dimensional funnel on an inclined plane. *The European Physical Journal B* **664**, 657–664 (1999).

22. Mersch, E., Lumay, G., Boschini, F. & Vandewalle, N., Effect of an electric field on an intermittent granular flow. *Physical Review E* **81**, 1–8 (2010).

23. Kubin, L. P. & Estrin, Y., The Portevin-Le Chatelier effect in deformation with constant stress rate. *Acta Metallurgica* **33**, 397–407 (1985).

24. Lebedkina, T. A. & Lebyodkin, M. A., Effect of deformation geometry on the intermittent plastic flow associated with the Portevin-Le Chatelier effect. *Acta Materialia* **56**, 5567–5574 (2008).

25. Penning, P., Mathematics of the portevin-le chatelier effect. *Acta Metallurgica* **20**, 1169–1175 (1972).

26. Glasser, B. J. & Goldhirsch, I., Scale dependence, correlations, and fluctuations of stresses in rapid granular flows. *Physics of Fluids* **13**, 407–420 (2001).

Methods

Numerical configuration The lattice is a two-dimensional square lattice with initial cell lengths l_0 and masses m at its vertices (see Fig. 1b). The springs transmit elastic forces to the masses; these masses carry a further dissipative force. We use a Verlet algorithm to integrate the mass motions at every time-step Δt.

The response of the spring elements follows the force-length diagram in Fig. 1c, which idealises the compaction response of a single puffed rice grain sustaining multiple breakages. The growths in both the stiffness and breakage strength are linear and follow the rules $k_{i+1} = k_i + ak_0$ and $F_{\mathrm{br}}^{i+1} = F_{\mathrm{br}}^i + aF_{\mathrm{br}}^0$, with $a = 0.01$ and i being the number of breakage events. The dissipative force that acts on the masses is given either by global or local viscous damping, or friction. Here we use global viscous damping to represent interactions with a background fluid at rest; at node j this force is calculated by ηv_j, where η is the viscosity and v_j is the nodal velocity. Use of either local damping or friction is discussed in Supplementary to further support the generality of our conclusions.

The relaxed lengths of the springs are initially set to be the distance between nodes. Nodes at the bottom boundary are fixed; along the sides nodes can move only vertically, and along the top they move at constant velocity V. As the lattice compresses, at some stage the springs start to break. A coarse-graining process is carried out to extract the velocity field following[26]. Results are presented non-dimensionally in terms of basic units of mass $[M] = m$, length $[L] = l_0$ and time $[T] = \Delta t$.

Definition of the breakage time In the model, spring breakage occurs every local strain $\frac{F_{\mathrm{br}}^i}{k_i l_i}$ and since the macroscopic strain rate $\frac{V}{H}$ in a non-breakable system is uniform with depth, we find $\tau_{\mathrm{br}}^i = \frac{F_{\mathrm{br}}^i}{k_i l_i} \frac{H}{V}$. Since the relaxed spring length, critical breakage force, and spring stiffness vary in time and space, it is convenient to define the initial breakage time: $\tau_{\mathrm{br}}^0 = \frac{F_{\mathrm{br}}^0}{k_0 l_0} \frac{H_0}{V}$

Correspondence should be addressed to I.E.

Author contributions

F.G, I.E. and L.S. conceived the model. F.G. performed model simulations. J.R.V. and I.E. conceived the experiments. P.G., J.R.V. and F.G. performed the experiments. All the authors contributed to the writing of the manuscript.

Supplementary material: Dynamic patterns of compaction in brittle porous media

François Guillard[1], Pouya Golshan[2], Luming Shen[1], Julio R. Valdes[2], and Itai Einav[1,3]

(Dated: June 26, 2015)

This supplementary section supports our proposition that the identified compaction patterns are characteristics of general brittle porous media involving two competing mechanisms: recurring fabric collapse (such as breakage or micro-buckling) and external dissipation (such as damping or friction). For example, in the model shown in the paper, mass motion is damped *via* global damping. To demonstrate that similar compaction patterns can be found as long as the model represents some form of external dissipation, we replace the global damping with either local damping or friction.

Local viscous damping is introduced as a force between node i with velocity $\mathbf{v}_i$ and node j with velocity $\mathbf{v}_j$, *i.e.* with a force $\eta(\mathbf{v}_j - \mathbf{v}_i)$ acting on node i and a force $\eta(\mathbf{v}_i - \mathbf{v}_j)$ acting on node j. Since in that case the viscosity operates at the spring level, the viscous time τ_η is no longer relevant, and is replaced by a Maxwell time $\tau_{\mathrm{m}} = \eta/k$ where k is the spring stiffness. Correspondingly, we define the non-dimensional group that reflects the action of external dissipation, *i.e.*, using

$$B_{\mathrm{m}} = \tau_{\mathrm{br}}/\tau_{\mathrm{m}}. \tag{S1}$$

Fig. S1a shows the corresponding phase diagram. Indeed, the diagram is essentially similar to the one found with global damping, though we note that the oscillatory compaction band regime extends to higher B_{m} than B_η, and that we could not detect more than two oscillatory compaction bands for the parametric range tested. Indeed, as we noted in the paper, bifurcation into more than one oscillatory compaction bands is reminiscent of critical phenomena near phase transitions, and its possible detection is highly delicate, either experimentally or computationally.

Next, we further study the effect of friction on the emergence of the various compaction regimes. Friction is here responsible for external dissipation due to interactions with the out of plane confining walls. It is therefore added to all the nodes, where each node can take a local frictional force in the opposite direction to its motion. The frictional force is proportional to the tangential displacement of that node, and we use a high tangential stiffness $k_t = 100$. If the calculated elastic tangential force is higher than μP, the force is set to μP, where μ is the friction coefficient and P is the pressure acting on the node through the forces in the springs connected to it. Fig. S1b shows the corresponding phase diagram. Unlike the previous cases with viscosity, the dimensionless number corresponding to internal dissipation is simply the friction coefficient μ. The phase diagram remains comparable to those observed in the viscosity cases, yet we could not detect more than two oscillatory compaction bands for the parametric range tested. Note that it is not possible to check whether the oscillatory compaction regime extends for higher friction coefficients μ, since in these cases the applied stress is screened through the medium (*viz.* the Janssen effect[1]) and only part of the sample is effectively compressed.
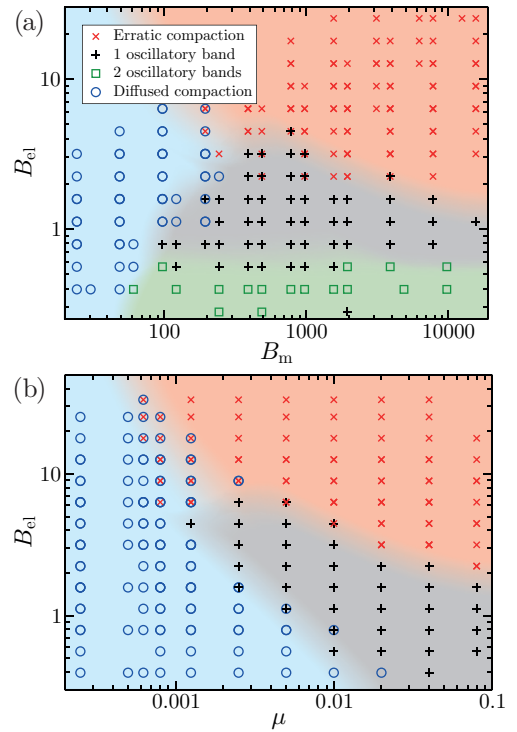

FIG. S1. Dimensionless phase diagram of compaction patterns with external dissipation *via*: (a) local viscous damping, (b) friction. Shadings highlight the various compaction regimes.

[1] Particles and Grains Laboratory, School of Civil Engineering, The University of Sydney, Sydney, NSW 2006, Australia.

[2] Geo-Innovations Research Lab; Department of Civil, Construction, and Environmental Engineering; San Diego State University.

[3] Dept of Civil, Environ & Geomatic Eng, Faculty of Engineering Science, University College London.

[1] Ovarlez, G., Fond, C. & Clément, E., Overshoot effect in the Janssen granular column: A crucial test for granular mechanics. *Physical Review E* **67**, 060302 (2003).